Featured in Physics

Porous-Solid Metaconverters for Broadband Underwater Sound Absorption and Insulation

Hao-Wen Dong,[1,*] Sheng-Dong Zhao,[2,†] Ping Xiang,[3] Bing Wang,[4] Chuanzeng Zhang,[5] Li Cheng,[6] Yue-Sheng Wang,[7] and Daining Fang[1,‡]

[1] *Institute of Advanced Structure Technology, Beijing Institute of Technology, Beijing 100081, China*
[2] *School of Mathematics and Statistics, Qingdao University, Qingdao 266071, China*
[3] *Systems Engineering Research Institute, Beijing 100094, China*
[4] *Luoyang Ship Material Research Institute, Luoyang 471023, China*
[5] *Department of Civil Engineering, University of Siegen, D-57068 Siegen, Germany*
[6] *Department of Mechanical Engineering, The Hong Kong Polytechnic University, Hong Kong, China*
[7] *Department of Mechanics, School of Mechanical Engineering, Tianjin University, Tianjin 300350, China*

(Received 9 December 2022; revised 3 February 2023; accepted 28 February 2023; published 25 April 2023)

Existing solid composite structures composed of several viscoelastic materials and metals mainly exploit diverse resonances, damping, and scattering to realize underwater acoustic wave functionalities. However, low-frequency broadband underwater sound absorption and insulation are still hard to capture with an acoustic coating possessing subwavelength thickness and lightweight nature simultaneously. This paper reports the systematic simulated and experimental validations of a porous-solid underwater metaconverter, consisting of a rubber layer and a topology-optimized elastic metasurface to exhibit broadband functionalities of sound absorption and insulation caused by the strong reflective and transmitted longitudinal-to-transverse wave conversion, while sustaining broadband impedance matching. Various results confirm the predicted capabilities of underwater broadband high-efficiency sound absorption (>80%) or insulation (20 dB) within the range of 2–10 kHz for a large- and limited-size sample, providing an estimate of the energy-converting effect and phenomenon. The present study provides possibilities for elastic wave energy dissipation, harvesting, and underwater acoustic stealth via metasurfaces.

DOI: 10.1103/PhysRevApplied.19.044074

I. INTRODUCTION

With the development of composite-material technology, underwater functional structural materials [1,2] have attracted much attention from various fields and showed great potential for versatile promising underwater applications. Based on empirical composite structures, traditional underwater acoustic technology mainly depends on the mechanisms of acoustic impedance matching [2], strong viscoelastic loss [3], active damping [4], enhanced wave scattering [5], or localized resonances [6] to realize effective underwater sound absorption [7]. In terms of the structural configuration [7], introducing filled particles, cavities, high-density rigid spheres, sandwich composites, gradient impedance, softly coated resonant units, or piezocomposite coatings [7] can give rise to efficient absorption. With suitable porosity, porous aluminum is produced [8] to achieve high underwater sound absorption (>80%) within the range of 15–30 kHz. When periodic acoustic structures are introduced, wave propagation is altered to enhance sound absorption. A kind of three-phase phononic crystal [9] supporting the local resonance is used for underwater absorption from 14.8 to 30 kHz. Based on multiple scattering theory, an underwater black-hole structure [10] is constructed to act as a kind of omnidirectional sound absorber within 10–40 kHz. Using a rubber and viscous matrix, a periodic bubble coating can create high underwater sound absorption (>97%) within 8–22 kHz [11]. By analyzing wave motion in multilayer viscoelastic materials, Sharma *et al*. [12] presented a rubber coating with periodic cavities and steel cylinders for near-perfect absorption through the combination of Fabry-Pérot and dipole resonances. Instead of columnar scatterers, periodic steel plates are embedded in the rubber matrix to act as a gradient broadband absorber for waterborne sound [13,14]. As for waterborne sound insulation [15], traditional sound-insulating materials usually include flexible soft media, such as rubber [15] and foam ingredients [16], that have very extremal density and acoustic velocity considerably smaller than those of the water. Hence, strong impedance

*hwdong@bit.edu.cn
†sdzhao@qdu.edu.cn
‡fangdn@bit.edu.cn

 © 2023 American Physical Society

mismatching can prevent energy transfer from structural vibrations to the fluid medium, thus reducing underwater radiation noise. Besides, the high-damping property [17] can suppress structural vibrations and then significantly reduce reflected energy from the interface between water and the structure. Based on the vibroacoustic coupled model, the analytical prediction and validation of noise reduction are presented by a decoupling layer made of viscoelastic materials and voids [18]. Using the equivalent fluid model, the optimized air cavities of the decoupling layer are used for sound insulation at 1500 Hz [19]. Considering the interaction between water and vibrations of the elastic structure, single and double microperforated plates can induce underwater peak sound absorption and insulation at different frequencies [17]. In view of commonly used materials with high damping and soft materials, existing sound absorption and insulation strategies still cannot reconcile high-efficiency energy dissipation and broadband perfect acoustic impedance matching with subwavelength load-bearing composite structures. This challenge induces further rigorous demands on the structural design and mechanism of wave manipulation.

Over the past decade, as artificial functional materials for the manipulation of waterborne acoustic waves, underwater acoustic metamaterials (UAMs) [7] can efficiently control the wave phase [20,21], amplitude [22], polarization [23], dispersion [23], and modes [23] through periodic or gradient elastic microstructures, while maintaining the desired engineered acoustic impedance. Consequently, the UAMs can give rise to waterborne acoustic absorption [2], insulation [24], focusing [25], and cloaking [1] with transform acoustics. Based on several local resonant [1] or gradient microstructures [23], the UAMs can achieve high sound absorption in a lower-frequency range than traditional absorbing materials. An acoustic metamaterial consisting of soft silicone rubber, polyurethane, and a steel core is designed to enable high absorption ($>70\%$) from 800 to 2500 Hz [6]. With similar multiple inclusions, a compound-lattice acoustic metamaterial composed of local resonant structures with a gradient woodpile configuration is constructed for high sound absorption from 2800 to 8800 Hz [26]. Since multiple-phase inclusions require high-precision manufacturing technologies and make the coating heavy and thick, metasurfaces with various local and Fabry-Pérot resonances are successively designed to reach broadband sound absorption. Recently, a composite metasurface made of pentamode materials and rubber-metal resonators was proposed to enable an average absorption of 87.8% within the range of 760–920 Hz. With a tungsten-polyurethane composite material, an underwater sound absorber is developed to possess broadband (4–20 kHz) impedance matching and integrated Fabry-Pérot resonances [2]. To pursue low-frequency underwater acoustic insulation, the UAMs utilize the local resonance, negative Poisson effect, chiral characteristics, and wave-front control to achieve the desired decoupling property for insulating noise induced by complex vibrations. Unlike traditional viscoelastic metal materials, a patterned bubble architecture is designed and fabricated to capture the ultrabroadband band gap for high-efficiency insulation [24]. With customized pentamode materials, the metasurface using the mechanism of propagating plane waves into evanescent waves is suggested to realize low-frequency insulation in an alternative approach [23]. Despite definite potential with respect to the aspects of low-frequency absorption and insulation, UAMs usually contain several high polymer materials and complicated metallic structures and still suffer from a series of issues, such as a relatively high working-frequency range, being overweight, cumbersomeness, multiple elaborately properad materials, single functionality, and hard to quantificationally control the waves. The core challenge for broadband underwater absorption and insulation is to customize elastic wave sound modes with strong energy dissipation and broadband impedance matching simultaneously.

To overcome the challenging integration of lightweight broadband sound absorption and insulation without multiphase solid inclusions using composite materials or structures, here, we report a lightweight underwater metaconverter composed of a rubber layer and porous-solid elastic metasurface, which can realize low-frequency broadband underwater high absorption and insulation. The heuristic genetic algorithm (GA) is utilized to inversely design a wave-conversion elastic metasurface that consists of periodic porous microstructures with strong anisotropy, which can effectively manipulate the transmitted and reflective elastic waves inside the metaconverter. Viscoelastic rubber with a customized elastic modulus and loss factor is fabricated to reduce interface reflection between water and the metaconverter as much as possible. Various wave characterization results show the expected broadband high-efficiency absorption and insulation. Energy characterization reveals that the metaconverter can support reflective longitudinal (L) to transverse (T) wave conversion. As a result, the T waves are trapped inside the rubber and metasurface. Meanwhile, the metaconverter can act as an effective shield with strong transmitted L-to-T wave conversion when the incident acoustic waves propagate through the metaconverter. Furthermore, underwater acoustic experiments demonstrate the functionalities of broadband sound absorption and insulation of the large- and limited-size sample. Our study demonstrates the potential of customized elastic wave control of a lightweight laminated structure and opens routes towards broadband multifunctional waterborne sound control using simple composite structures.

This paper is organized as follows. Section II presents the design concept, characterization of the rubber layer, and wave responses of the metaconverter. To explore the underling physics, Sec. III first presents the mechanistic

analysis of underwater sound absorption from the energies of the metaconverter. Then, detailed energy characterization is conducted for the mechanism of underwater sound insulation. Subsequently, the experimental results and corresponding analyses are proposed in Sec. IV. Finally, Sec. V highlights the main contributions of the study and gives the future challenges of underwater metaconverters.

II. DESIGN AND CHARACTERIZATION OF UNDERWATER METACONVERTERS

In the underwater acoustic environment, the focus of manipulating acoustic and elastic waves lies in constructing specific viscoelastic materials and metals to utilize the strong coupling between the waves and solid microstructures. Here, Fig. 1 presents a porous-solid underwater metaconverter, in which the 2-cm-thick rubber layer is attached to the surface of the 2-cm-thick periodic elaborative anisotropic metallic microstructures [27]. For this kind of inhomogeneous anisotropic solid medium, the equation of motion, constitutive equation, and expressions of strain are described by

$$\sigma_{ij,j} = \rho_{ij}\ddot{u}_j, \tag{1}$$

$$\sigma_{ij} = C_{ijkl}\varepsilon_{kl}, \tag{2}$$

and

$$\varepsilon_{kl} = (u_{k,j} + u_{l,k})/2, \tag{3}$$

where σ is the stress, ρ_{ij} is the density tensor, u denotes the displacement, and ε is the strain.

The corresponding wave equation of the anisotropic medium is written as

$$C_{ijkl}u_{l,jk} = \rho_{ij}\ddot{u}_j. \tag{4}$$

The plane harmonic bulk wave form is defined as

$$u_i = U_i \exp[ik(n_j x_j - v)], \tag{5}$$

where U_i is the amplitude of the particle displacement, k is the wave number, n_j is the wave-propagation vector, and v is the phase velocity. By substituting Eq. (5) into Eq. (4), the Christoffel equation for bulk waves in anisotropic elastic solids can be expressed as

$$(C_{ijkl}n_k n_j - v^2\rho_{il})U_l = 0, \tag{6}$$

where C_{ijkl} indicates the elastic modulus tensor. If $C_{ijkl}n_k n_j = \Lambda_{il}$, the phase velocities of different wave modes can be solved by

$$|\Lambda_{il} - v^2\rho_{il}| = 0. \tag{7}$$

For the viscoelastic rubber layer, the constitutive relationship can be written as

$$\sigma_{ij} = \psi_{ijkl} * \dot{\varepsilon}_{kl}, \tag{8}$$

where ψ_{ijkl} is the component of the fourth-order tensor relaxation function, and * indicates the time convolution.

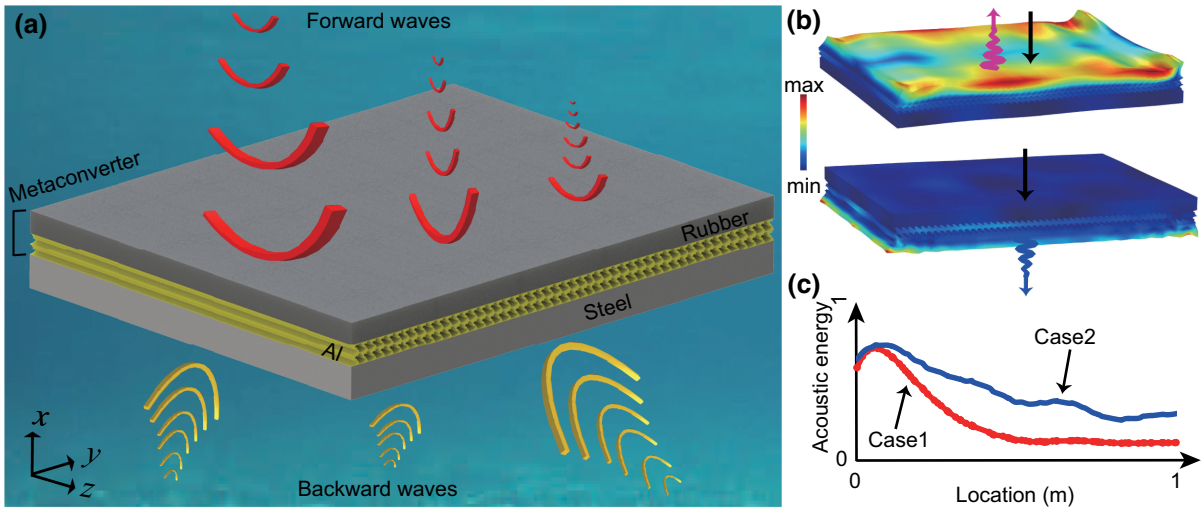

FIG. 1. Schematic of a double-layer underwater metaconverter. (a) Illustration of the metaconverter, consisting of a rubber layer (2 cm) and elastic metasurface made of aluminum (2 cm). Metaconverter fixed on steel backing (3 cm) can absorb most of the energy of the incident forward waves or isolate the energy of incident backward waves below the steel backing. (b) Sketch of the vibration modes of the rubber layer to enable sound absorption (upper) or sound insulation (lower). (c) Transmission spectra of L and T waves through the rubber layer with density = 950 kg/m^3, Poisson ratio = 0.49, Young's modulus = 1.4×10^8 Pa, and structural loss factor = 0.2. Background solids without damping have the same material (density, Poisson ratio, and Young's modulus) parameters as rubber. Dimensions of the metasurface microstructure along the x, y, and z directions are 1, 1, and 50 cm, respectively.

For the isotropic viscoelastic medium, the wave equation can be given as

$$\nabla[(\lambda^* + 2\mu^*)(\nabla \cdot \tilde{\mathbf{u}})] - \nabla \times [\mu^* \nabla \times \tilde{\mathbf{u}}] + \rho\omega^2 \tilde{\mathbf{u}} = 0, \tag{9}$$

where λ^* and μ^* are the first- and second-order complex Lame constants.

When the metaconverter is surrounded by water, the time-harmonic steady-state response is formulated as

$$\begin{bmatrix} \mathbf{K}_s - \omega^2 \mathbf{M}_s & -\mathbf{H} \\ \rho_f \omega^2 \mathbf{H}^T & \mathbf{K}_f - \omega^2 \mathbf{M}_f \end{bmatrix} \begin{bmatrix} \mathbf{u} \\ p \end{bmatrix} = \begin{bmatrix} F_s \\ F_f \end{bmatrix}, \tag{10}$$

where $\mathbf{K}_s$ is the stiffness matrix of the elastic domain, $\mathbf{M}_s$ is the elastic mass matrix, $\mathbf{K}_f$ is the stiffness matrix for the fluid domain, $\mathbf{M}_f$ is the fluid mass matrix, $\mathbf{u}$ is the displacement vector of the solid, p is the acoustic pressure of water, F_s denotes the fluid force exerted on the structure, and F_f represents the force from the structure acting on the fluid.

In addition, the wave equation of the fluid without viscosity is given by

$$\nabla \left[\frac{1}{\rho} \nabla p \right] = -\frac{1}{\rho c_l^2} \omega^2 p, \tag{11}$$

where p is the pressure, and c_l is the longitudinal wave velocity of the fluid.

The nongradient topology optimization [23] is utilized to inversely design the elastic metasurface with anisotropic microstructures for the targeted frequency range $[f_{\min}, f_{\max}]$. To realize the prescribed effective intrinsic parameters $(C_{11}^T, C_{66}^T, C_{16}^T, \rho^T)$ of a microstructure, it is necessary to minimize the difference between the retrieval effective parameters $(C_{11},\ C_{66},\ C_{16},\ \rho)$ and the target ones through changing the material distribution of the microstructure. Considering the possible manufacturing requirements, the optimization problem, consisting of the specific objective function and constraints, is formulated as follows:

$$\text{for } f_i = [f_{\min}, f_{\max}],\ (i = 1, 2, \ldots N_F), \tag{12}$$

$$\text{minimize } O(\Omega_D) = \max \left\{ \left[\frac{\max\limits_{\forall i}(C_{11}(i), C_{11}^T)}{\min\limits_{\forall i}(C_{11}(i), C_{11}^T)} \right], \left[\frac{\max\limits_{\forall i}(C_{66}(i), C_{66}^T)}{\min\limits_{\forall i}(C_{66}(i), C_{66}^T)} \right], \left[\frac{\max\limits_{\forall i}(C_{16}(i), C_{16}^T)}{\min\limits_{\forall i}(C_{16}(i), C_{16}^T)} \right], \left[\frac{\max\limits_{\forall i}(\rho(i), \rho^T)}{\min\limits_{\forall i}(\rho(i), \rho^T)} \right] \right\}, \tag{13}$$

$$\text{subject to } \rho_i = \{0, 1\}, (i = 1, 2, \ldots N \times N), \tag{14}$$

$$\min_{\Omega_D}(w) \geq w_0, \tag{15}$$

where the targeted range is $[f_{\min}, f_{\max}] = [0.5\text{ Hz}, 10\text{ kHz}]$, with N_F sampling frequencies; Ω_D denotes the design domain (microstructure); O is the objective function; ρ_i indicates the material distribution of every element of a microstructure [0 (1) for vacuum (solid)]; w is the width array containing the widths of all local solid blocks; and w_0 means the prescribed minimal size (a/40) of solids, where a is the lattice constant of a microstructure. To allow strong enough anisotropy, it is assumed that the microstructure has no symmetry. Every microstructure is treated as an individual in GA. Then, the microstructure is meshed to 80×80 finite elements (pixels) during optimization. First, the initialized population, with $N_p = 90$ individuals, is generated randomly. To avoid the checkerboard pattern and reduce the isolated island parts, a modified "abuttal entropy filter" [23] method is applied to improve the topology of a microstructure. Then, the fitness of every individual is determined according to Eq. (13). Combined with Eq. (15), the tournament selection strategy with a size of competition group of $N_{\text{TS}} = 45$ is applied to the current population for reproduction. Subsequently, the genetic operations of crossover with probability $P_c = 0.9$ and mutation with probability $P_m = 0.02$ are adopted to create the offspring population. Finally, the typical single-elitism strategy is used to accelerate convergence and avoid the degeneration of evolution. If the fixed number (2000) of evolution generation is reached, the algorithm produces the desired anisotropic microstructure possessing the targeted effective parameters within the given frequency range. Otherwise, another round of genetic operations will be executed

for the next generation until the terminal condition is met.

As shown in Fig. 1(a), when the microstructure with $(C_{11}, C_{66}, C_{16}, \rho) = (C_{11}^0, C_{11}^0, 0.98C_{11}^0, \rho^0)$ is designed, the elastic metasurface can immensely alter one bulk wave mode to form another one, where C_{11}^0 represents the elastic longitudinal modulus of aluminum (2.368×10^9 Pa) and ρ^0 is 950 kg/m^3. The acoustic impedance of this metasurface can match with that of water. Fixed on a steel-backing plate, the metaconverter can absorb the forward incident acoustic waves efficiently. Meanwhile, the backward incident waves also can be isolated by the metaconverter significantly, and thus, prevent the propagation of acoustic waves. The underwater sound absorption in one direction and sound insulation in the other direction aim at two different potential application requirements, i.e., high absorption can deal with the external active sonar detection, but high insulation is responsible for the internal noise leakage. Regarding the reduction of the threats of noise on people, it requires airborne-sound noise reduction or noise shielding, which are different from the underwater sound insulation considered herein.

As displayed in Fig. 1(b), when the acoustic wave is incident on the rubber-layer surface, the excited elastic waves are transmitted into the porous-solid layer and subsequently reflected by the steel backing. Then the elastic waves excite the complex vibrations of the rubber layer, which can convert the wave energy into thermal energy for the energy dissipation through the suitable vibration modes. The dominant physics lies in the reflective L-to-T wave conversion. When the acoustic waves are incident below the steel backing, the whole metaconverter can give rise to wave isolation, which benefits from the complex vibration modes preventing propagated acoustic plane waves. Moreover, Fig. 1(c) illustrates that the rubber layer can absorb more energy of the T wave than that of the L wave. When the T wave is excited from the background solid, the T wave will propagate through the rubber layer and be dissipated to a great extent as well. However, most energy from the T wave can transmit into the background solid, while little energy is absorbed by rubber. With the increase of frequency, the difference between the transmission of T and L waves enlarges to about 0.6 gradually. Overall, the present porous-solid metaconverter can lead to three kinds of mechanics, i.e., the reflective (transmitted) L-to-T wave conversion, the dissipation of viscoelastic solid materials, and the impossibility of supporting the T wave by water. In particular, the dominant working mechanism is L-to-T wave conversion, which enables broadband high-efficiency absorption (insulation) using only materials with a small loss factor (0.2). It is the ability and flexibility of manipulating the near-field acoustic waves by customized polarization and dissipation that helps the metaconverter in Fig. 1 to realize effectual underwater sound absorption and insulation simultaneously.

Compared with Ref. [27], the present study presents the following five contributions: (1) utilizing a three-dimensional (3D) finite-size structure instead of a two-dimensional (2D) infinitely periodic model; (2) analyzing quantitatively the different wave motions brought about by the transformation from 2D to 3D design; (3) realizing the integration of sound absorption and insulation, rather than sound absorption only; (4) revealing the mechanism of compatible reflective and transmitted wave conversion for incorporating sound absorption and insulation, and providing alternative knowledge and a strategy for waterborne sound-insulation technology; and (5) conducting underwater acoustic experiments, in addition to theory and simulation analyses.

To more clearly illustrate L-to-T wave conversion, we investigate the propagation characteristics of L and T waves based on the solid-solid model shown in Fig. 2, i.e., the scattering features of the reflection and transmission cases. When the model in Fig. 2(a) is considered, the scattering matrix for reflection can be obtained by

$$\begin{bmatrix} u_{x,0}^r \\ u_{y,0}^r \end{bmatrix} = \begin{bmatrix} S_{LL} & S_{TL} \\ S_{LT} & S_{TT} \end{bmatrix} \begin{bmatrix} u_{x,0}^i \\ u_{y,0}^i \end{bmatrix}, \tag{16}$$

where S_{LL}, S_{TL}, S_{LT}, and S_{TT} are the scattering parameters; $u_{x,0}^r(u_{x,0}^i)$ and $u_{y,0}^r(u_{y,0}^i)$ are the displacements of reflective (incident) wave fields along the x and y directions, respectively. Similarly, when the model in Fig. 2(c) is considered, the corresponding scattering matrix of transmission is defined by

$$\begin{bmatrix} u_{x,0}^t \\ u_{y,0}^t \end{bmatrix} = \begin{bmatrix} S_{LL}^* & S_{TL}^* \\ S_{LT}^* & S_{TT}^* \end{bmatrix} \begin{bmatrix} u_{x,0}^i \\ u_{y,0}^i \end{bmatrix}, \tag{17}$$

where S_{LL}^*, S_{TL}^*, S_{LT}^*, and S_{TT}^* are the scattering parameters; $u_{x,0}^t$ and $u_{y,0}^t$ are the displacements of transmitted wave fields along the x and y directions, respectively.

As shown in Fig. 2(b), the incident L waves can induce reflective T and L waves obviously. At most frequencies, the amplitudes of reflective T waves are larger than those of reflective L waves. The maximal reflective L-to-T conversion occurs at 2900 Hz. The vibration mode in Fig. 2(e) shows the nature of transverse motion for the rubber layer clearly. In addition, Fig. 2(d) also illustrates the similar strong transmitted L-to-T conversion induced by the metasurface. The maximal transmitted L-to-T conversion occurs at 2000 Hz. Therefore, L-to-T wave conversion occurs due to the metasurface with anisotropic microstructures.

For the working principle of the underwater metaconverter, strong mode conversion dominates the wave propagation of elastic and waterborne acoustic waves based on the dynamic damping of viscoelastic material. Taking

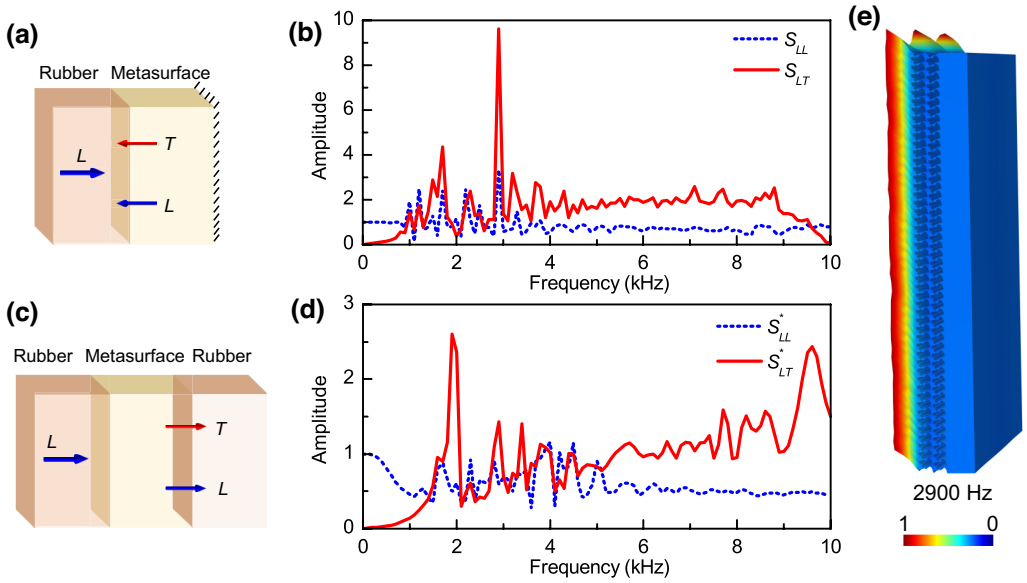

FIG. 2. Elastic scattering features and transverse-wave motion induced by mode conversion, considering the periodic boundary condition. Model (a) and scattering parameters S_{LL} and S_{LT} (b) for wave reflection. Model (c) and scattering parameters S^*_{LL} and S^*_{LT} (d) for wave transmission. (e) Vibration mode at 2900 Hz for wave reflection with maximal conversion. Nonreflecting and fixed boundary conditions are applied on the left and right edges of the model in (a). Nonreflecting boundary conditions are applied on the left and right edges of the model in (c). Color represents the displacement amplitude.

advantage of the extreme anisotropy of the microstructures, the metasurface can evoke strong reflective (transmitted) L-to-T wave conversion. When the forward acoustic waves strike on the rubber layer, the L waves can be dramatically converted into reflective T waves. There are multiple reflections in the two-layer system with limited size. Meanwhile, the rest of the L waves are dissipated by the rubber layer. In particular, water cannot support the propagation of T waves, and the T waves can be dissipated by rubber strongly. When the backward acoustic waves strike the steel backing, the transmitted L-to-T wave conversion can produce many T waves. Part of the L waves will be reflected into water. The other part will be dissipated by the rubber layer. In a word, the reflective and transmitted L-to-T wave conversion in the porous-solid metaconverter gives rise to the broadband high-efficiency sound absorption and insulation, respectively.

To confirm the underwater acoustic wave functionalities of the metaconverter under the condition of the finite structure size, Fig. 3(a) shows the static and dynamic mechanical characterization of the metaconverter by dynamic mechanical analysis. The tensile storage modulus of the fabricated rubber increases linearly with frequency. Its loss factor, however, increases from 0.2 to 0.25 first, and then decreases to approximately 0.05. In fact, this is the typical frequency-temperature characteristic of a viscoelastic material. The loss capacity of a polymer material is related to temperature and frequency. When the temperature increases gradually, the motor ability of the molecular segments increases gradually. Meanwhile, the loss factor reaches a maximum around the glass transition temperature, because internal loss caused by the movement of the molecular-chain segment is the largest at this time. According to the time-temperature equivalence principle of polymers, increasing the temperature is equivalent to reducing the frequency. Therefore, the loss factor can reach a maximum at a certain frequency (about 10 Hz herein). Some detailed explanations can be found in a standard book [28] on the subject.

Therefore, the loss factor is more susceptible to the working frequency. The absorption coefficient, A, is defined as

$$A = 1 - T^2 - R^2, \tag{18}$$

where T and R are the amplitudes of the transmitted and reflected acoustic pressures, respectively. The models for absorption and insulation using the metaconverter are shown in Fig. 3(b). With the same thickness of rubber layer, the metaconverter can still maintain broadband excellent absorption if the measured material parameters of the rubber are considered. Even though the loss factor becomes small, the absorption at high frequency (8–10 kHz) is very close to that with constant parameters, see Fig. 3(c). So, the metaconverter can realize sound absorption exceeding 80% within a broadband frequency range, if the rubber adopts a constant tensile modulus (140 MPa) and loss factor (0.2). When the rubber layer is thicker, the metaconverter maintains broadband and high-efficiency features, showing the strong robustness of

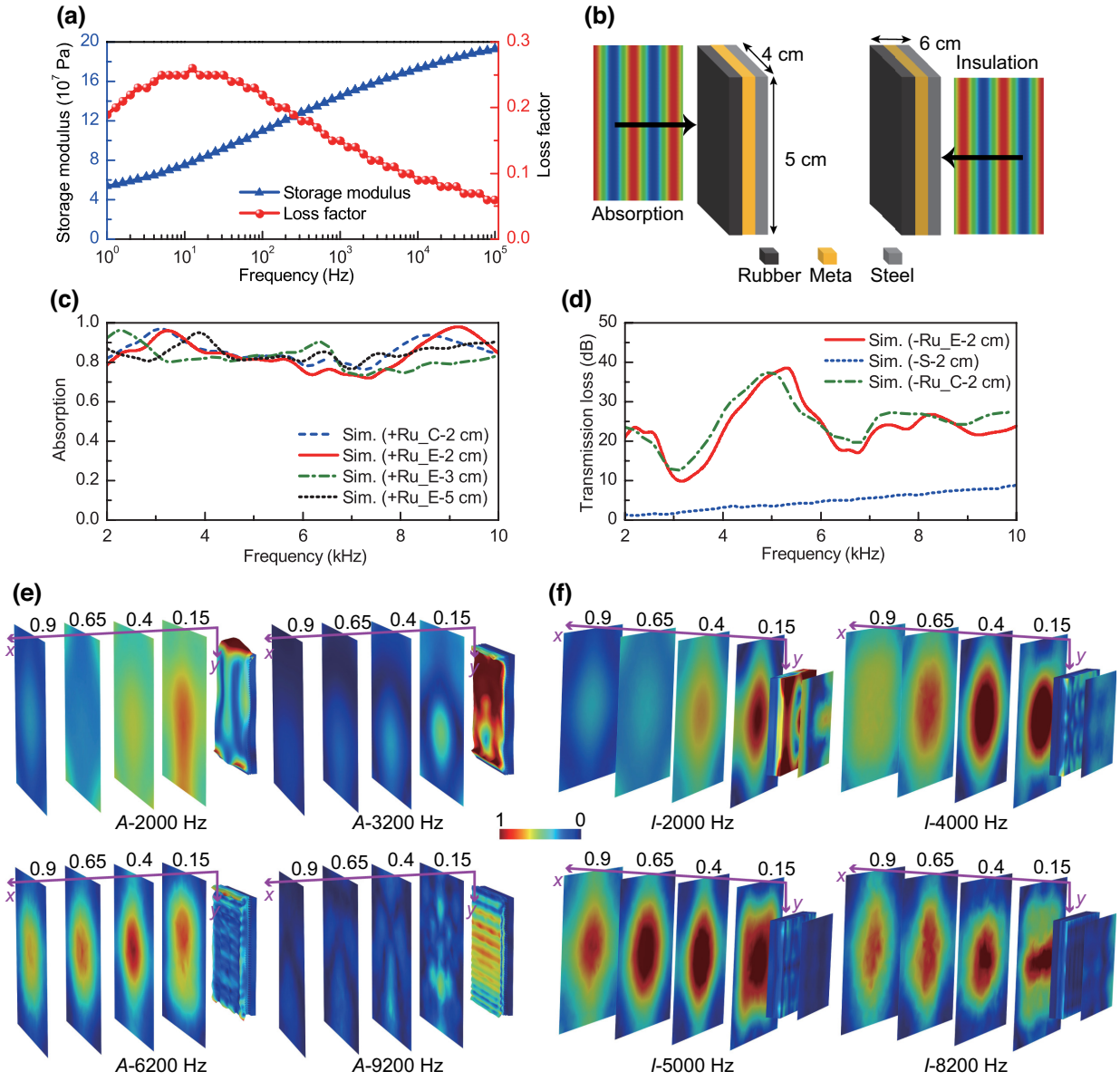

FIG. 3. Dynamic properties and wave responses of the metaconverter. (a) Measured frequency-dependent storage modulus and loss factor of the rubber by dynamic mechanical analysis testing. (b) Simulation model for characterizing sound absorption (left) and insulation (right) of the double-layer metaconverter. All thicknesses of the rubber, metasurface, and steel layers are 2 cm. Left and right models represent forward (+) and backward (−) incidences, respectively. (c),(d) Sound absorption and insulation curves with different material parameters and incident waves. Both the constant (Ru_C) and measured frequency-dependent (Ru_E) moduli are adopted to characterize the property of the rubber layer. Simulation based on steel backing (S) is also presented for comparison. Simulated acoustic pressure and total displacements fields at representative frequencies within 2000–10 000 Hz for sound absorption (e) and insulation (f). Fields are extracted from the results using 2-cm-thick rubber with measured parameters in (a).

the metaconverter. To characterize sound insulation, the transmission loss is defined as

$$\mathrm{TL} = 20\ \log_{10}(1/T^2). \tag{19}$$

As shown in Fig. 3(d), the transmission loss of the metaconverter using different parameters of the rubber layer is superior to that of the steel plate. It is observed that the transmission loss is lower than 5 dB in the frequency range of 2–6 kHz. Therefore, the pure-steel backing cannot effectively isolate the acoustic wave in an underwater environment. Figure 3(d) presents simulation curves of the metaconverter with two kinds of parameters of rubber, i.e., one has a constant modulus and loss factor, and the other one uses the measured modulus and loss factor depicted in Fig. 3(a). When the metaconverter with

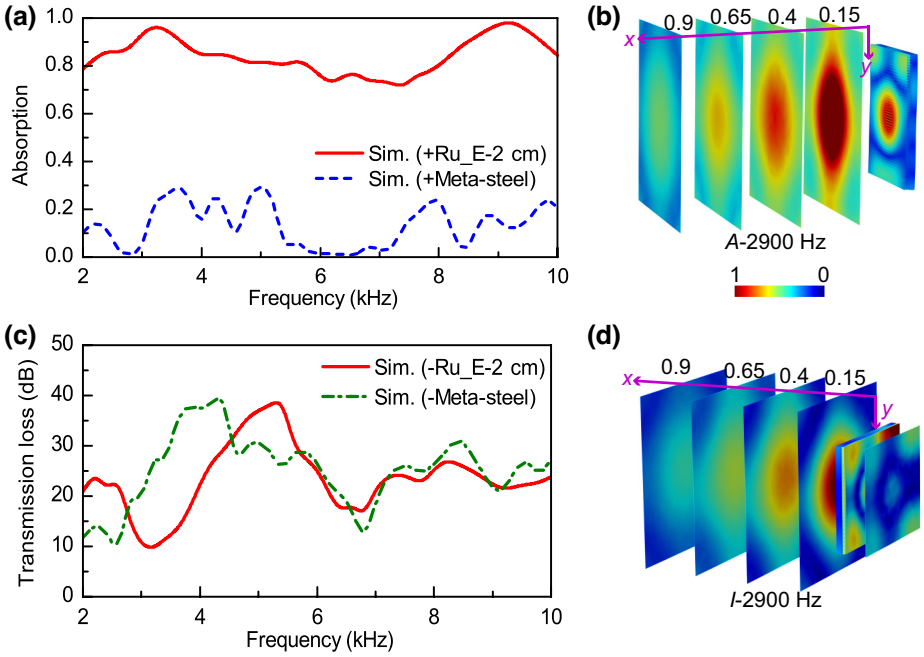

FIG. 4. Sound absorption and insulation of the model without a rubber layer. (a),(b) Absorption curve (+Meta-steel) and acoustic field of the model containing only rubber and steel backing. (c),(d) Insulation curve (−Meta-steel) and acoustic field of the model containing only the metasurface and steel backing. For comparison, the results of the metaconverter (+Ru_E-2 cm, −Ru_E-2 cm) are presented as well.

either constant or frequency-dependent material parameters is introduced, the system can obtain broadband effective (>20 dB) sound insulation. This further illustrates that the resulting functionalities by the metaconverter are not sensitive to changes to the rubber parameters. It also means that the manufacturing of a metaconverter is less demanding. To intuitively verify sound absorption and insulation, Figs. 3(e) and 3(f) present the numerically simulated acoustic and elastic fields (pressure and displacement) at four representative frequencies. The reflected pressure amplitudes at 2, 3.2, and 9.2 kHz are smaller than those at 6.2 kHz, which coincide with the simulation absorption curve in Fig. 3(c). Larger vibration amplitudes of the rubber layer usually lead to a higher absorption efficiency. As shown in Fig. 3(d), the waves transmitted through the metaconverter provoke complex vibrations of the rubber layer, where the energy is dissipated at 2 kHz. As a result, the acoustic energy near the rubber surface is significantly reduced for sound insulation. However, the reflected acoustic fields and elastic fields at 4, 5, and 8.2 kHz are similar to each other, i.e., the vibration amplitude of rubber is not strong, while most of the energy

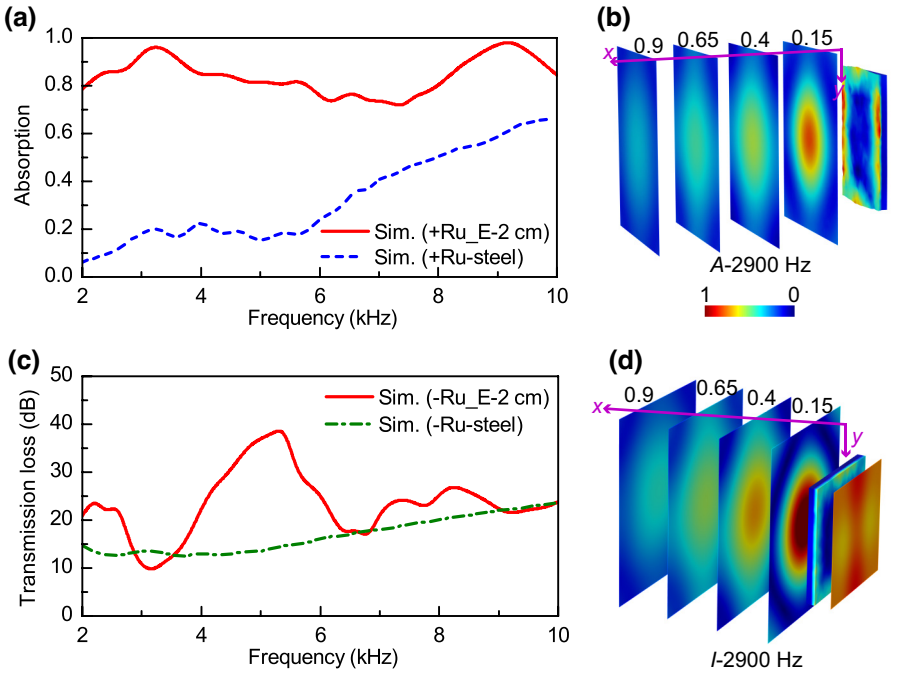

FIG. 5. Sound absorption and insulation of the model without a metasurface layer. (a),(b) Absorption curve (+Ru-steel) and acoustic field of the model containing only rubber and steel backing. (c),(d) Insulation curve (−Ru-steel) and acoustic field of the model containing only rubber and steel backing. For comparison, the results of the metaconverter (+Ru_E-2 cm, −Ru_E-2 cm) are presented as well.

is reflected. Therefore, it is impedance mismatching that leads to high-performance sound insulation. In short, the 4-cm-thick metaconverter can realize effective underwater sound absorption (>72.7%) and insulation (>9.4 dB) in the same broad frequency range of 2–10 kHz.

To check the contribution of each layer to sound absorption and insulation, Figs. 4 and 5 illustrate the absorption and insulation performances of the model without a rubber layer (Fig. 4) or a metasurface layer (Fig. 5). Figure 4(a) shows that the model without a rubber layer has a small absorption over the whole frequency range. The absorption performance is nowhere near that of the metaconverter model. However, the model without a rubber layer also shows satisfactory sound insulation, the low-frequency performance of which is worse than that of the metaconverter model, see Fig. 4(c). The strong reflected acoustic field in Fig. 4(b) and high-transmission field in Fig. 4(d) confirm low sound absorption and insulation.

Figure 5(a) shows that the sound absorption is smaller than 50% within the range of 2–8 kHz. Because of the damping nature of rubber, the absorption becomes larger above 8 kHz, but still smaller than 80%. Similarly, the sound-insulation ability of the metaconverter is superior to that of the model with rubber and steel backing within the ranges of 2–2.9 and 3.7–10 kHz, as shown in Fig. 5(c). In addition, the responses in Figs. 5(b) and 5(d) show obvious reflection and transmission without apparent transverse motions of the rubber layer. Therefore, wave conversion by the metasurface can effectively improve sound absorption and insulation within the low- and medium-frequency ranges.

To summarize, only the combination of the porous-solid metasurface layer and rubber layer can implement broadband high-efficiency sound absorption and insulation. But the reflective (transmitted) L-to-T wave conversion is the dominant mechanism of wave functionalities.

To check the angle of the reflective acoustic wave, Fig. 6 displays the scattering properties of the acoustic wave reflected from the metaconverter. As shown in Figs. 6(a) and 6(b), all reflective acoustic waves within the broad range of 2–10 kHz are located along the normal direction, although a little energy propagates along the other directions. Figure 6(c) further intuitively shows that the region with the maximal wave amplitude points to the direction of 180°. So, the irregular and anisotropic solid structure cannot change the angle of the reflective wave.

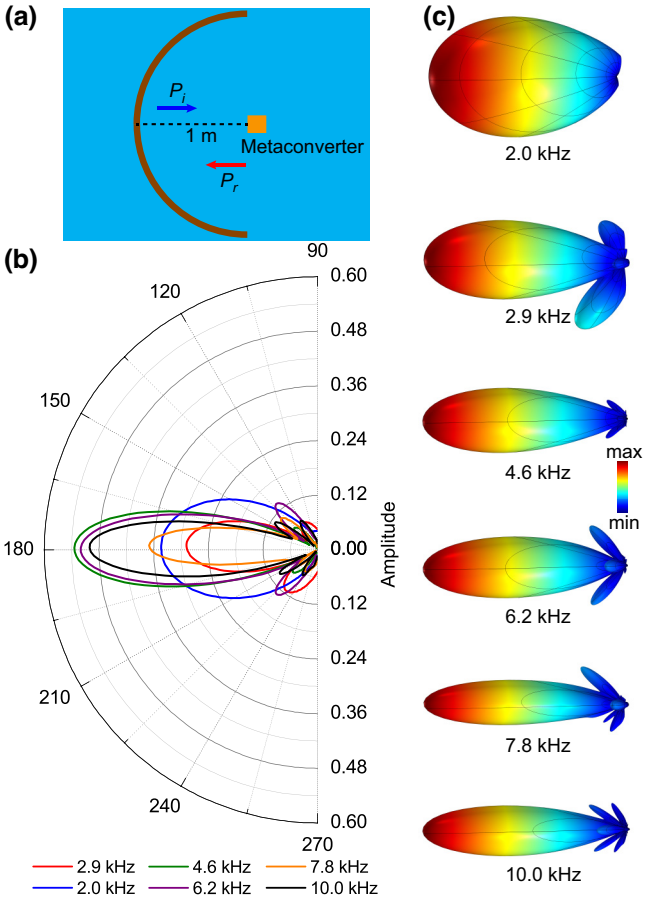

FIG. 6. Scattering property of acoustic wave fields. (a) Schematic of the model for scattering characterization. Response is extracted from the semicircle 1 m from the metaconverter. (b) Acoustic pressure distribution in polar coordinates. (c) Acoustic scattering maps at representative frequencies.

III. MECHANISMS OF BROADBAND SOUND ABSORPTION AND INSULATION

To expound the elastic bulk wave conversion in the metaconverter, this section shows the quantitative characterization of the elastic wave energies in the system. Since the metaconverter is surrounded by water, fluid-structure coupling boundary conditions are imposed on the interface between water and the solid. Acoustic radiation boundary conditions are applied on the outermost boundary of the water region to eliminate boundary reflection. To obtain the steady-state response, the background acoustic field is applied in the water region on the left side of the rubber layer. After sweeping the frequencies, the resulting broadband frequency-domain response is achieved. Under the response of absorption or insulation simulation, the energy densities of L and T waves can be further evaluated by calculating the resulting displacement fields and intrinsic parameters of materials.

For the isotropic solid material (rubber and aluminum), the corresponding strain-energy densities of L-wave and T-wave modes are defined as

$$\tilde{e}_L(x,t) = \frac{1}{2V}\sum_{x,t}[(\lambda+2\mu)(\nabla\cdot\mathbf{U})(\nabla\cdot\mathbf{U})], \tag{20}$$

$$\tilde{e}_T(x,t) = \frac{1}{2V}\sum_{x,t}[\mu(\nabla\times\boldsymbol{U})(\nabla\times\boldsymbol{U})], \tag{21}$$

where V is the volume of occupied space of the medium; $\tilde{e}_L$ and $\tilde{e}_T$ represent energy densities; x and t are the location and time, respectively; λ and μ are the Lamé constants, and $\mathbf{U}$ is the displacement vector. Although Eqs. (20) and (21) cannot represent the energies of pure L and T waves, they characterize the dominant L-wave and T-wave modes of the solid materials, thus showing the definite physical meaning.

In general, the incident acoustic wave can induce reflective L and T waves. As shown in Figs. 7(a) and 7(b), the L- and T-wave energies are calculated and integrated over the occupied volume of the rubber and elastic metasurface, respectively. Figures 7(c) and 7(d) show the corresponding energy fields at representative frequencies of Figs. 7(a) and 7(b). Figure 7(a) shows that the energy of the L-wave mode is much smaller than that of the T-wave mode at almost all frequencies, except those around 7 kHz. Similarly, the energies of the T-wave mode are 700–1000 times those of the L-wave mode, as shown in Fig. 7(b). Obviously, these big differences indicate the occurrence of L-to-T wave conversion in both the rubber and metasurface layers. However, the variation tendency of the T-wave mode in the rubber layer is contrary to that in the metasurface layer. It is speculated that the opposite feature is caused by the different boundaries of the two layers. As illustrated in Fig. 7(c), the T-wave energy of the rubber layer at 2.2 kHz is maximal and localized on the boundaries. Meanwhile the L-wave energy at 2.2 kHz is nearly zero. The T-wave energy is only localized on the upper boundary and smaller than the T-wave one at 7.2 kHz. This shows that wave conversion of the rubber layer makes the T-wave localized, thus leading to broadband high-efficacy sound absorption.

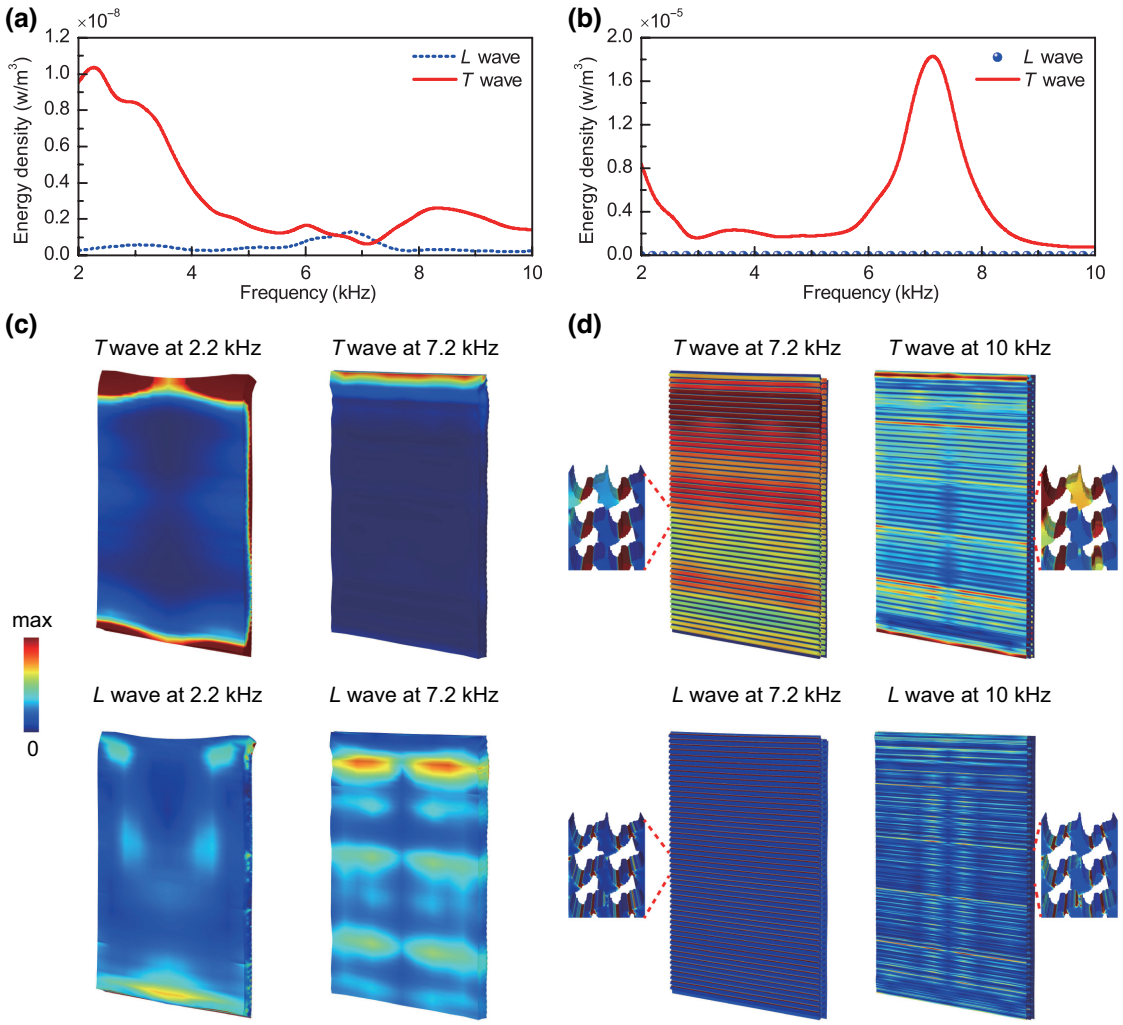

FIG. 7. Characterization of wave energy inside the metaconverter for sound absorption. Strain energies of L- ($\tilde{e}_L$) and T-wave ($\tilde{e}_T$) modes inside the rubber layer (a) and elastic metasurface (b). Energy fields of the rubber layer (c) and elastic metasurface (d) at several representative frequencies. Four inserted pictures show the enlarged local fields of the metasurface. Most of T- and L-wave energies are mainly located in the small solid blocks and thin connections, respectively.

From the energy fields in Fig. 7(d), the *T*-wave energy of the metasurface at 7.2 kHz becomes maximal and much larger than that of the *L*-wave one, which is mainly localized at the solid connections. However, the *T*-wave energy is spread over the whole metasurface. The small *L*-wave energy at 10 kHz localizes at the connection components, but the *T*-wave energy localizes at the upper and lower edges. This signifies that the combination of the converted *T*-wave energy distributed in the metasurface and the localized *T*-wave energy of the rubber layer can significantly improve sound absorption.

Similarly, Fig. 8 shows the energy performances of *L*- and *T*-wave modes inside the metaconverter when the incident backward waves are insulated. It is observed from Figs. 8(a) and 8(b) that both the rubber layer and elastic metasurface support the evident *T*-wave energy that is much larger than the *L*-wave energy. Since the effective acoustic impedance of the metasurface varies from $1.001Z_0$ to $1.018Z_0$, where Z_0 is the impedance of water, the broadband sound insulation is apparently caused by strong wave conversion instead of impedance mismatching, i.e., the incident acoustic wave will stimulate *T* waves in the metasurface because most of the wave energy cannot propagate through the metaconverter, thus giving rise to high-efficiency broadband sound insulation. Figure 8(c) indicates that the *T*-wave energy is localized at the corners at 2 kHz. However, the *L*-wave energy is relatively disperse at the same frequency. When the frequency increases to 6.8 kHz, the *T*-wave energy of the rubber layer is more concentrated than that of the *L* wave one. This suggests that the localization of the *T*-wave energy at the boundaries is beneficial for sound insulation. For the metasurface shown in Fig. 8(d), homoplastically, the *T*-wave energy is focused at the boundaries, but the *L*-wave energy

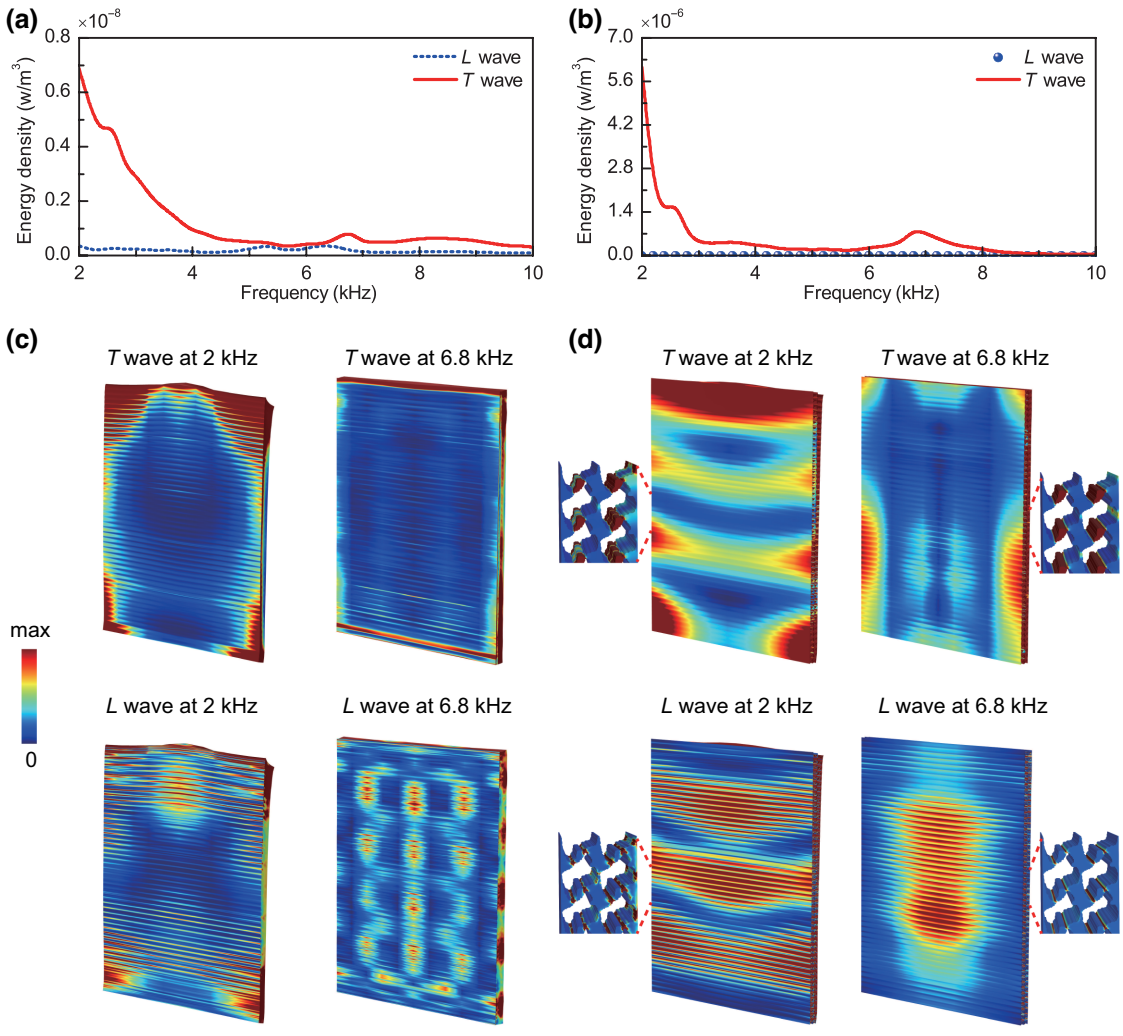

FIG. 8. Characterization of wave energy inside the metaconverter for sound insulation. Strain energies of two wave modes inside the rubber layer (a) and elastic metasurface (b). Energy fields of the rubber layer (c) and elastic metasurface (d) at several representative frequencies. Four inserted pictures show enlarged local fields of the metasurface. Like the distributions in Fig. 7(d), most of the *T*- and *L*-wave energies are mainly located in the small solid blocks and thin connections, respectively.

is mainly distributed in the middle region. Obviously, this distribution difference can also contribute to sound insulation. Therefore, the metaconverter can induce both reflective *L*-to-*T* wave conversion (Fig. 7) and transmissive *L*-to-*T* wave conversion (Fig. 8), while maintaining ideal broadband impedance matching. As a result, the metaconverter can support broadband sound absorption and insulation.

As shown in Figs. 7 and 8, there is a huge difference between the energy density in the rubber layer and in the metasurface. This clearly indicates that most *L*- and *T*-wave energies are trapped in the metasurface. The residual *L* and *T* waves can be further dissipated by the rubber layer. Since the *T* waves cannot propagate into water, the resulting underwater sound reflection of the metaconverter will be very small and even near zero.

In fact, the contribution of rubber includes three aspects: (1) guaranteeing impedance matching to completely guide the *L* waves into the metaconverter, (2) dissipating the *L* and *T* waves, and (3) introducing the multiple reflection of *T* waves. It is noted that wave conversion cannot be perfect, as shown in Fig. 2. Although the rubber layer does not store and dissipate much wave energy, the resulting absorption and insulation ability will be significantly degraded if the residual *L* waves cannot be dissipated. Considering practical applications, the combination of rubber and metasurface layers is more meaningful.

To be honest, it is hard to quantificationally show the dissipation extent of the wave energy in rubber. As illustrated in Fig. 9, if the loss factor of the rubber layer is removed, the resulting absorption and insulation performances of the model are significantly degenerate, especially for absorption. This laterally indicates that the damping nature of the viscoelastic material can contribute to dissipating the wave energy to realize high-efficiency sound absorption and insulation.

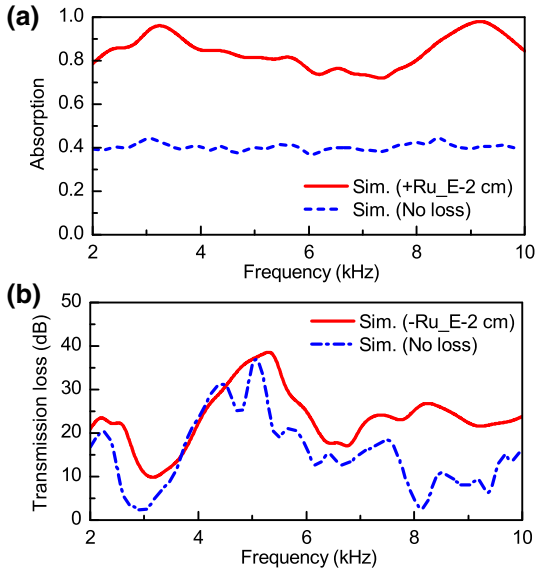

FIG. 9. Sound absorption and insulation of the metaconverter without loss. (a) Absorption curve (No loss) of the model in which rubber has no loss factor. (b) Insulation curve (No loss) of the model in which rubber has no loss factor. For comparison, the results of the metaconverter (+Ru_E-2 cm, −Ru_E-2 cm) are presented as well.

The partial wave energy in Figs. 7 and 8 is concentrated near the edges of the structure. This feature is caused by the finite-size effect. It is worth mentioning that some energy is also located at the edges of the structure shown in Figs. 5(b) and 5(d). However, sound absorption and insulation are very small because no wave conversion is involved when the metasurface layer is removed. More exactly, the energy distribution in Figs. 7 and 8 is dominated by the *L*-to-*T* wave conversion, in association with a certain contribution from the finite-size effect. Of course, this means that the metaconverter is very robust because the finite structural effect is not considered during design.

IV. EXPERIMENTAL VALIDATION OF UNDERWATER METACONVERTERS

To validate the aforesaid concept and design, we conduct detailed underwater sound experiments with a large- and finite-size metaconverter, as shown in Fig. 10(a). The porous-solid layer is fabricated by wire-electrode cutting. The styrene-butadiene rubber layer is created by vulcanization. The metaconverter is attached to a steel plate by adhesive glue. Note that there are no air gaps between the two interfaces. They are connected to each other through the strong waterproof glue. Moreover, if air gaps exist in the interface between the rubber layer and metasurface, the incident acoustic wave will be markedly reflected into the water region, resulting in a low-absorption ability. If there are air gaps in the interface between the metasurface and steel backing, sound insulation will be inefficient. Unlike the acoustic tube test for the small-size sample, the pulse method is utilized to measure the transmission, reflection, and absorption of a large-sized sample in the anechoic pressure cylinder shown in Fig. 10(b). The measured absorption is superior to the simulated curve in the range of 2–8 kHz, but it shows a lower absorption from 8 to 10 kHz, see Fig. 10(c). Since the viscosity of water can improve the absorption efficiency to a certain extent, the experimental results implicitly introduce viscosity and show a better performance than the simulated ones. Comfortingly, the measured insulation curve in Fig. 10(d) surpasses the simulated one over the whole frequency range of interest. Note that there are visible differences over the whole frequency range. We speculate that a certain wave diffraction ascribed to the limited size of the sample may cause some differences of about 10 dB in the low-frequency range.

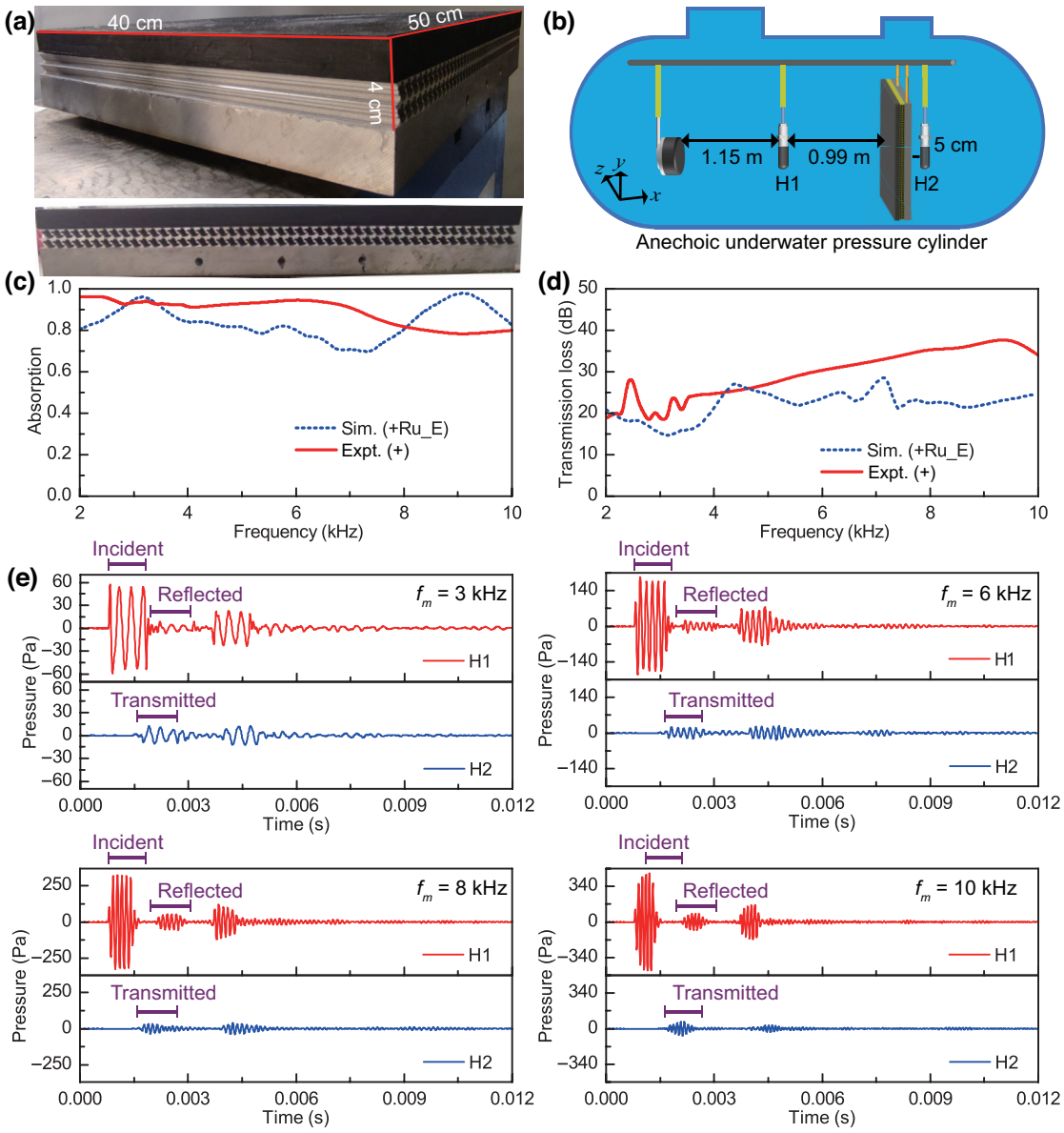

FIG. 10. Measured underwater acoustic functionalities of the metaconverter. (a) Sample with a rubber layer ($40 \times 50 \times 2$ cm^3) and an aluminium plate ($40 \times 50 \times 2$ cm^3), which is attached to the steel backing ($40 \times 50 \times 3$ cm^3). Two side views of the sample and local enlarged picture are displayed. (b) Underwater experimental sets. Two hydrophones are marked by H1 and H2, respectively. Signal is generated by the underwater transducer in front of H1 and received by H1 and H2. Measured (expt.) and simulated (sim.) sound-absorption coefficients (c) and sound-transmission-loss coefficients (d). Acoustic waves incident from the left side of the rubber layer for cases of both sound absorption and insulation. (e) Measured time-domain results at four representative incident pulse signals with center frequencies of 3 kHz, 6, 8, and 10 kHz.

From the application perspective, the steel backing can be taken as the shell of underwater vehicle or equipment itself. So, the steel backing doesn't belong to a part of the underwater acoustic coating which only contains the rubber layer and metasurface. In this case, the coating can be called the lightweight structure/material. Because its apparent density is consistent with that of water, being superior to some existing multimaterial acoustic coatings.

To directly show the whole propagation process of the acoustic signals, Fig 10(e) illustrates the signals at hydrophones H1 and H2 at four representative frequencies. The reflected pressure amplitude is much smaller than the incident one at 3 kHz, while the transmissive pressure amplitude is very small as well. This performance matches with the absorption of 90% and transmission loss of 20 dB in Figs. 10(c) and 10(d). When the frequency

increases to 6 kHz, the reflected and transmissive pressure amplitudes are smaller, showing the high-efficiency absorption and insulation. When the frequency changes to 8 and 10 kHz, the absorption becomes lower, while the insulation is improved. Note that the better performance of the experimental results may benefit from the viscosities of water and the bonding material in the interfaces. Because it is not easy to measure these viscosities, the simulations do not introduce these special parameters.

In reality, the pressure cylinder is filled with water when the underwater acoustic experiment is conducted. So, no water-air interface exists during the experiment, which is different from the water-tank experiment. As shown in Fig. 11, to clarify the source of wave signals, it is effective to calculate the time of arrival for every signal based on the primary distances and acoustic velocity of water, i.e., the time of arrival for the nonstop signal is $t_1 = 0.77$ ms, the time of arrival for the signal reflected from the sample is $t_2 = 2.09$ ms, and the time of arrival for the signal reflected from the round surface is $t_3 = 3.716$ ms. Therefore, the signals after the reflected signal are cause by the reflection of the round surface of the pressure cylinder. It is the superposition [Figs. 11(b) and 11(c)] of omnidirectional reflected signals that result in a much higher amplitude than the reflected signal.

Overall, the underwater acoustic experiments validate the high-efficiency absorption and insulation of the double-layer inverse-design metaconverter from 2 to 10 kHz. Besides, from the trends of curves in Figs. 10(c) and 10(d), we can speculate that the metaconverter can possess similar functionalities at lower frequencies if a larger-sized sample can be designed and fabricated.

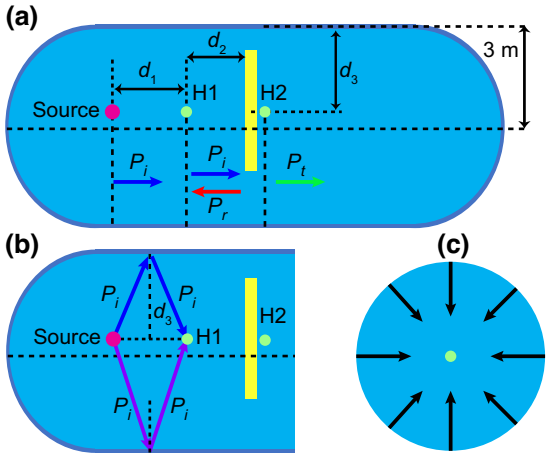

FIG. 11. Schematic of propagation of wave signals. (a) Dimensions of the pressure cylinder. (b),(c) Ways wave signals reflect. Primary values are $d_1 = 1.15$ m, $d_2 = 0.99$ m, and $d_3 = 2.72$ m.

V. CONCLUSIONS

Unlike existing UAMs for absorption or insulation, an inverse-design metaconverter made of elaborate porous solids combined with a rubber layer is proposed to enable broadband high-efficiency sound absorption and insulation. The underlying reflective L-to-T wave conversion enables high-efficiency (>80%) absorption in the low-frequency broadband range. Meanwhile, a similar transmitted L-to-T wave conversion leads to effective sound insulation (>20 dB) within the same range as well. The present underwater lightweight metaconverter has the advantages of being lighter, with low-frequency and absorption-insulation integration, than previous underwater acoustic metamaterials. From the perspective of manufacturing, more importantly, the metaconverter significantly moderates the customization demands of viscoelastic polymer materials. Various simulations substantiate the obvious phenomenon of wave conversion in the metaconverter. The effects of broadband low-echo and low-entrant sound are also observed through the underwater acoustic experiments. Although faced with strong coupling at the interface between water and the finite-sized structure, the metaconverter can well sustain the underwater acoustic stealth performance and then show strong robustness. In a future study, a larger design space for this kind of metaconverter is feasible for a lower-frequency and thinner coating. Of course, the effect and mechanism of hydraulic pressure on the metaconverter also need to be studied in depth. In short, the present porous-solid metaconverter may provide possibilities for customized elastic wave control [29–31] and acoustic wave engineering [7,32].

ACKNOWLEDGMENTS

This work is supported by the National Natural Science Foundation of China (Grants No. 52250217, No. 12172044, and No. 11972246) and the Beijing Institute of Technology Research Fund Program for Young Scholars. H.W.D. would like to thank Dr. Bin Wu (National University of Ireland, Galway, Ireland) for his helpful discussions.

H.-W.D., conceptualization, methodology, formal analysis, visualization, writing–original draft; S.-D.Z., methodology, formal analysis, data curation, visualization, discussion, validation; P.X., materials processing, discussion; B.W., materials processing, discussion; C.Z., discussion, writing–review and editing; L.C., discussion, writing–review and editing; Y.-S.W., discussion, writing–review and editing; D.F., supervision, writing–review and editing, project administration.

The authors declare that they have no known competing financial interests or personal relationships that could have appeared to influence the work reported in this paper.

[1] S. Zhang, C. Xia, and N. Fang, Broadband Acoustic cloak for ultrasound waves, Phys. Rev. Lett. **106**, 024301 (2011).

[2] S. Qu, N. Gao, A. Tinel, B. Morvan, V. Romero-García, J. P. Groby, and P. Sheng, Underwater metamaterial absorber with impedance-matched composite, Sci. Adv. **8**, eabm4206 (2022).

[3] Y. Li, F. Xu, Z. Lin, X. Sun, Q. Peng, Y. Yuan, S. Wang, Z. Yang, X. He, and Y. Li, Electrically and thermally conductive underwater acoustically absorptive graphene/rubber nanocomposites for multifunctional applications, Nanoscale **9**, 14476 (2017).

[4] T. R. Howarth, V. K. Varadan, X. Bao, and V. V. Varadan, Piezocomposite coating for active underwater sound reduction, J. Acoust. Soc. Am. **91**, 823 (1992).

[5] Y. Zhang and J. Pan, Underwater sound scattering and absorption by a coated infinite plate with a distributed inhomogeneity, J. Acoust. Soc. Am. **133**, 2082 (2013).

[6] H. Meng, J. Wen, H. Zhao, and X. Wen, Optimization of locally resonant acoustic metamaterials on underwater sound absorption characteristics, J. Sound Vib. **331**, 4406 (2012).

[7] E. Dong, P. Cao, J. Zhang, S. Zhang, N. X. Fang, and Y. Zhang, Underwater acoustic metamaterials, Natl. Sci. Rev., nwac246 (2022).

[8] G. Cheng, D. He, and G. Shu, Underwater sound absorption property of porous aluminum, Colloids Surf., A **179**, 191 (2001).

[9] H. Zhao, Y. Liu, J. Wen, D. Yu, and X. Wen, Tri-component phononic crystals for underwater anechoic coatings, Phys. Lett. A **367**, 224 (2007).

[10] C. J. Naify, T. P. Martin, C. N. Layman, M. Nicholas, A. L. Thangawng, D. C. Calvo, and G. J. Orris, Underwater acoustic omnidirectional absorber, Appl. Phys. Lett. **104**, 073505 (2014).

[11] V. Leroy, A. Strybulevych, M. Lanoy, F. Lemoult, A. Tourin, and J. H. Page, Superabsorption of acoustic waves with bubble metascreens, Phys. Rev. B **91**, 020301 (2015).

[12] G. S. Sharma, A. Skvortsov, I. MacGillivray, and N. Kessissoglou, Sound absorption by rubber coatings with periodic voids and hard inclusions, Appl. Acoust. **143**, 200 (2019).

[13] Y. Zhang, J. Pan, K. Chen, and J. Zhong, Subwavelength and quasi-perfect underwater sound absorber for multiple and broad frequency bands, J. Acoust. Soc. Am. **144**, 648 (2018).

[14] Y. Zhang and L. Cheng, Ultra-thin and broadband low-frequency underwater acoustic meta-absorber, Int. J. Mech. Sci. **210**, 106732 (2021).

[15] S. H. Sohrabi and M. J. Ketabdari, Stochastic modeling and sensitivity analysis of underwater sound absorber rubber coating, Appl. Acoust. **164**, 107282 (2020).

[16] M. Ates, S. Karadag, A. A. Eker, and B. Eker, Polyurethane foam materials and their industrial applications, Polym. Int. **71**, 1157 (2022).

[17] H. S. Kim, P. S. Ma, B. K. Kim, S. R. Kim, and Y. H. Seo, Underwater sound absorption and insulation of elastic micro-perforated plates in impedance tubes, Appl. Acoust. **197**, 108935 (2022).

[18] M. Tao, W. L. Tang, and H. X. Hua, Noise reduction analysis of an underwater decoupling layer, J. Vib. Acoust. **132**, 061006 (2010).

[19] L. Huang, Y. Xiao, J. Wen, H. Zhang, and X. Wen, Optimization of decoupling performance of underwater acoustic coating with cavities via equivalent fluid model, J. Sound Vib. **426**, 244 (2018).

[20] K. Melde, A. G. Mark, T. Qiu, and P. Fischer, Holograms for acoustics, Nature **537**, 518 (2016).

[21] X. Wu, X. Xia, J. Tian, Z. Liu, and W. Wen, Broadband reflective metasurface for focusing underwater ultrasonic waves with linearly tunable focal length, Appl. Phys. Lett. **108**, 163502 (2016).

[22] Z. Ren, H. W. Dong, X. He, M. Chen, and D. Fang, Underwater gradient metalens for broadband subwavelength focusing, Int. J. Mech. Sci. **229**, 107521 (2022).

[23] H. W. Dong, S. D. Zhao, X. B. Miao, C. Shen, X. Zhang, Z. Zhao, C. Zhang, Y. S. Wang, and L. Cheng, Customized broadband pentamode metamaterials by topology optimization, J. Mech. Phys. Solids **152**, 104407 (2021).

[24] Z. Cai, S. Zhao, Z. Huang, Z. Li, M. Su, Z. Zhang, Z. Zhao, X. Hu, Y. S. Wang, and Y. Song, Bubble architectures for locally resonant acoustic metamaterials, Adv. Funct. Mater. **29**, 1906984 (2019).

[25] X. Su, A. N. Norris, C. W. Cushing, M. R. Haberman, and P. S. Wilson, Broadband focusing of underwater sound using a transparent pentamode lens, J. Acoust. Soc. Am. **141**, 4408 (2017).

[26] H. Jiang, Y. Wang, M. Zhang, Y. Hu, D. Lan, Y. Zhang, and B. Wei, Locally resonant phononic woodpile: A wide band anomalous underwater acoustic absorbing material, Appl. Phys. Lett. **95**, 104101 (2009).

[27] H. W. Dong, S. D. Zhao, M. Oudich, C. Shen, C. Zhang, L. Cheng, Y. S. Wang, and D. Fang, Reflective Metasurfaces with Multiple Elastic Mode Conversions for Broadband Underwater Sound Absorption, Phys. Rev. Appl. **17**, 044013 (2022).

[28] M. Rubinstein, *Ralph, Polymer Physics* (Oxford University Press, Oxford, United Kingdom, 2003), pp. 76. ISBN 978-0-19-852059-7.

[29] H. W. Dong, S. D. Zhao, Y. S. Wang, and C. Zhang, Topology optimization of anisotropic broadband double-negative elastic metamaterials, J. Mech. Phys. Solids **105**, 54 (2017).

[30] A. O. Krushynska, V. G. Kouznetsova, and M. Geers, Visco-elastic effects on wave dispersion in three-phase acoustic metamaterials, J. Mech. Phys. Solids **96**, 29 (2016).

[31] H. Lee, J. K. Lee, H. M. Seung, and Y. Y. Kim, Mass-stiffness substructuring of an elastic metasurface for full transmission beam steering, J. Mech. Phys. Solids **112**, 577 (2018).

[32] H. W. Dong, C. Shen, S. D. Zhao, W. Qiu, H. Zheng, C. Zhang, S. A. Cummer, Y. S. Wang, D. Fang, and L. Cheng, Achromatic metasurfaces by dispersion customization for ultra-broadband acoustic beam engineering, Natl. Sci. Rev. **9**, nwac030 (2022).